A specific 3D shell approach for textile composite reinforcements under large deformation

Renzi Bai, Julien Colmars, Naïm Naouar, Philippe Boisse

Composites: Part A 139 (2020) 106135

Contents lists available at ScienceDirect

Composites Part A

journal homepage: www.elsevier.com/locate/compositesa

A specific 3D shell approach for textile composite reinforcements under large deformation

Renzi Bai, Julien Colmars, Naim Naouar, Philippe Boisse *

Université de Lyon, LaMCoS, CNRS, INSA-Lyon, F-69621, France

ARTICLE INFO

Keywords:
A. Fabrics/textiles
A. Layered structures
C. Finite element analysis (FEA)
E. Forming
Fibrous shell

ABSTRACT

The deformation of textile composite reinforcements is strongly conditioned by their fibrous composition. Standard plate and shell theories are based on kinematic assumptions that are not verified for textile reinforcements. A 3D shell approach specific to fibrous reinforcements is proposed. It is based on two specificities: the inextensibility of the fibres and the possible slippage between the fibres. The approach is developed in a continuum-based shell element. The form of the virtual work reflects the specificities of the deformation of the fibrous reinforcements. It takes into account the tensile and bending stiffness of the fibres. Friction between fibres is taken into account in a simple way in connection with bending. The present approach is based on the actual physics of the deformation of the textile reinforcements. It makes it possible to simulate the 3D deformations of textile reinforcements and provides displacements and strains for all points in the fabric thickness and the proper rotations of the material normal.

1. Introduction

The use of composite materials has led to weight reductions and consequently decrease in fuel consumption in the transport industry, particularly in the aeronautical and automotive sectors. Composites can be adapted so that their characteristics meet the intended applications. However, the manufacturing processes to obtain these materials are complex and achieving a defect-free composite part is a difficult challenge. To enable the increasing use of composite materials, it is necessary to replace costly development with experimental methods based on trial and error by optimising manufacturing parameters by means of simulations and virtual manufacturing. The manufacture of textile-reinforced composites often requires the preforming of a dry textile reinforcement and the subsequent injection of a resin in LCM processes (Liquid Composite Moulding) [1–3]. The composite can also be produced by thermoforming a prepreg consisting of a textile reinforcement incorporating the unhardened matrix, so that the composite can be formed [4–8]. In both cases (LCM and prepreg), the forming process is driven by the deformation of the textile reinforcement. The basic physics of the deformation is the same and is that of the deformation of textile reinforcement made of continuous fibres.

Kinematic drape models were the first approaches developed for the simulation of the forming of woven textile reinforcements [9–12]. These methods are purely geometric and are fast. However, they do not take into account the mechanical behaviour of the materials or the exterior loads on the reinforcements. In view of the low bending stiffness of textile reinforcements, some membrane approaches have been proposed [13–17]. They neglect the bending stiffness. They take into account the in-plane mechanical behaviour of the fabric, in particular the in-plane shear behaviour which is specific and has a major importance in draping. Nevertheless, it has been shown that bending stiffness has an important role during draping. In particular, it conditions the onset of wrinkling and the size of the wrinkles [18,19]. Taking bending stiffness into account is not straightforward. A standard shell approach gives a bending stiffness that depends on the membrane rigidities and the thickness. This leads to a bending stiffness that is much too large for the textile reinforcement. This is due to the fibrous composition of the reinforcement, which makes slippage possible between the fibres. This is an important point that is taken into account in this article. Several approaches have been proposed to address this difficulty. Textile reinforcement can be considered as a laminate material with different thickness properties that can be adjusted to achieve both correct membrane and bending stiffnesses [20–24]. Stress resultant shell approaches that relate the resulting forces along a normal (Tensile and shear forces, bending moments) to membrane and bending strains naturally decouple membrane and bending stiffnesses [25,26]. Finally, the combination of a

* Corresponding author.
E-mail address: philippe.boisse@insa-lyon.fr (P. Boisse).

https://doi.org/10.1016/j.compositesa.2020.106135
Received 5 July 2020; Received in revised form 17 September 2020; Accepted 19 September 2020
Available online 28 September 2020

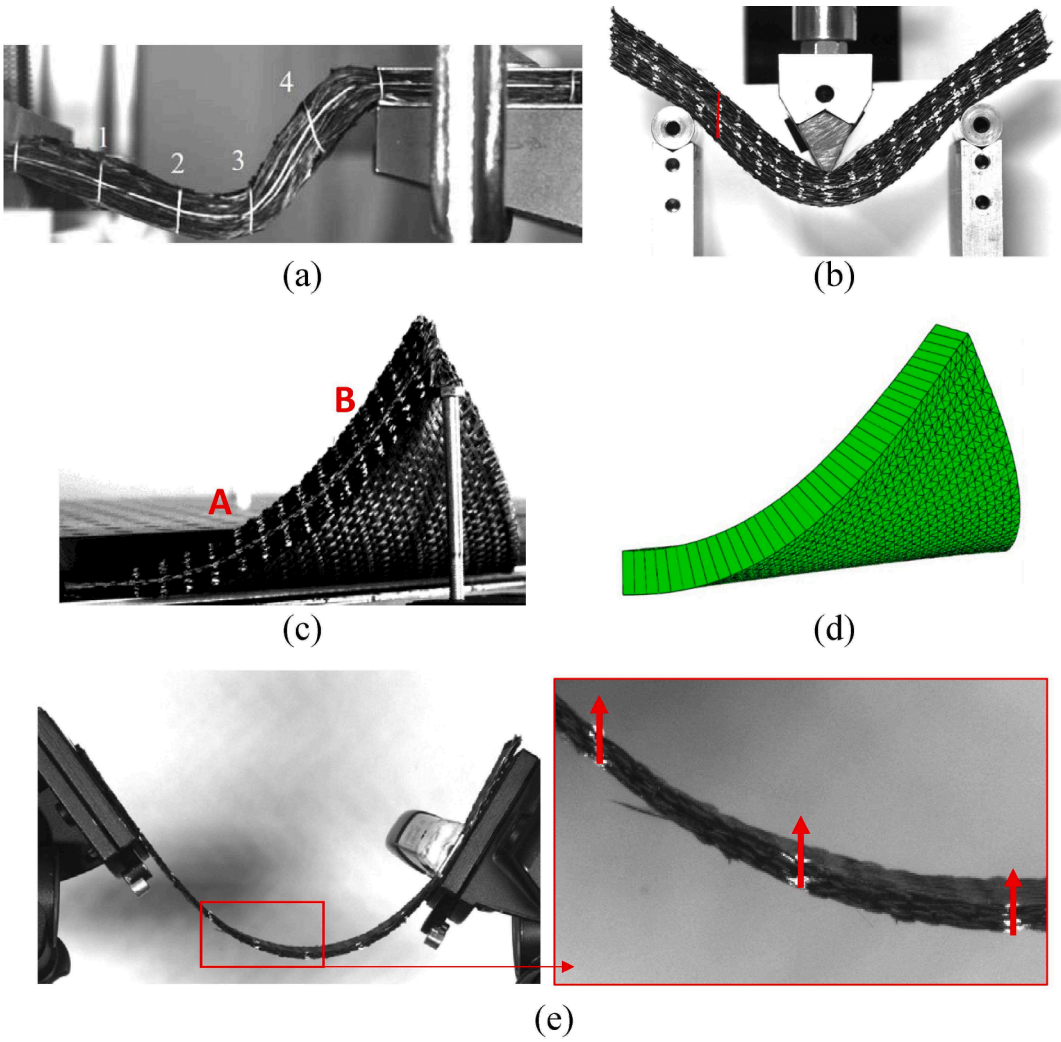

Fig. 1. (a) Bending experiment of multilayer reinforcements; (b) 3 points bending test of multilayer reinforcement; (c) 3D Bending due to an imposed displacement at the corner; (d) Simulation using Mindlin shell S3 element in Abaqus; (e) Bending of a thin reinforcement. (For interpretation of the references to colour in this figure legend, the reader is referred to the web version of this article.)

bending finite element (e.g. DKT) with a membrane finite element is also used [27,28].

These different methods make it possible to decouple the membrane deformation energy from the bending energy. However, some aspects are artificial, and these methods are not based on the physics of the deformation of a textile reinforcement. Moreover, they do not provide the displacements and strains for points in the thickness of the fabric. Verification of the inextensibility of the fibres is not assured and the rotations of the material normals, which are related to this inextensibility, are not known correctly. The approach that is proposed in this article has this objective: to define a 3D shell approach, specific to fibrous reinforcement, which gives the displacements and strain in any point of the textile reinforcement as well as the rotation of the material normals (This is what a shell theory does). It will be shown that standard shell approaches such as Kirchhoff and Mindlin are not relevant for fibrous reinforcements. The proposed specific shell approach is based on the quasi-inextensibility of the fibres and the possibility of slippage between the fibres. These two points are the major specificities of the physics of the deformation of a fibrous reinforcement. The feasibility of the approach in the case of a 2D two node fibrous element in the plane has been presented in [29]. The aim of the present article is to develop an approach to simulate all cases of 3D deformation of textile reinforcements. The formulation is implemented in the framework of the 3D continuum-based shell elements [30–32]. It concerns both thin and thick textile reinforcements. Simulations of large deformations of textile reinforcements in 3D cases are presented and validated by comparisons with experiments.

2. Specificities of the mechanical behaviour of fibrous materials

Plate and shell approaches concern solids whose geometry is close to a middle surface and thin enough to simplify the kinematics i.e. it depends on a smaller number of variables than 3D solids. In an orthogonal coordinate system of x,y,z coordinates, a plate is considered to have a thickness h and a middle surface z = 0. The displacements along x,y,z, and the components of the rotation from the normal to the plate are noted u,v,w, and θ_x, θ_yrespectively. The hypothesis is made that the points along a segment oriented by the normal initially perpendicular to the middle surface remain on a straight segment that consists of the deformed normal. Consequently:

$$\begin{bmatrix} u \\ v \\ w \end{bmatrix} = \begin{bmatrix} \overline{u} \\ \overline{v} \\ \overline{w} \end{bmatrix} + z \begin{bmatrix} \theta_y \\ -\theta_x \\ 0 \end{bmatrix} \tag{1}$$

Here $\overline{u}, \overline{v}, \overline{w}$ are the displacements of the point of the middle surface. The strains are as follows:

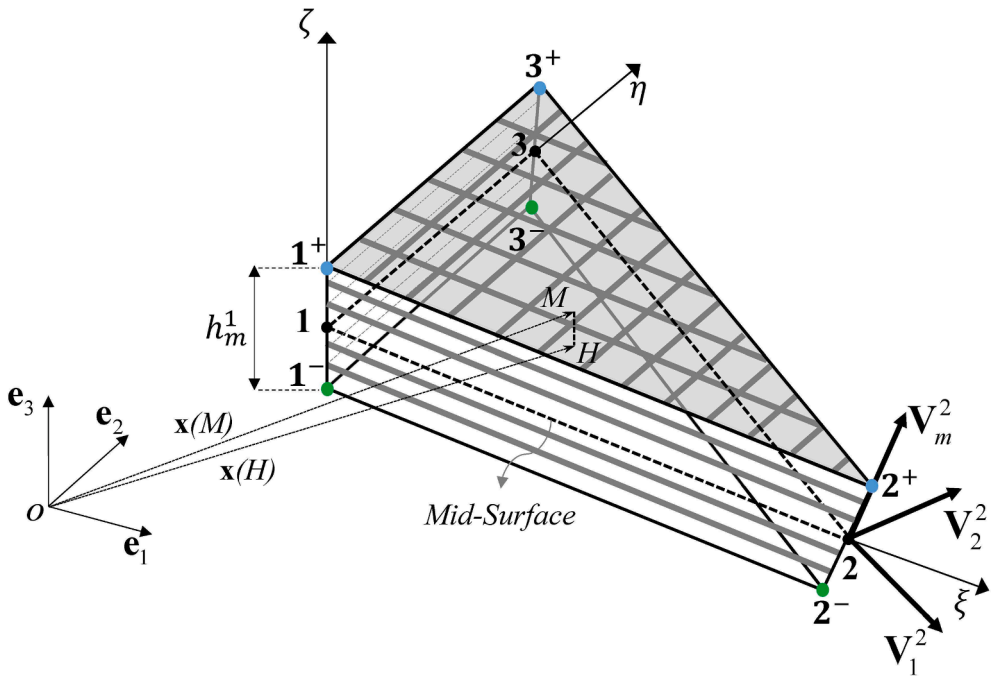

Fig. 2. Geometry of the 3D fibrous shell element. (For interpretation of the references to colour in this figure legend, the reader is referred to the web version of this article.)

$$\boldsymbol{\varepsilon} = \boldsymbol{e} + z\boldsymbol{\chi} \qquad \varepsilon_{xz} = \frac{1}{2}\gamma_{xz} \qquad \varepsilon_{yz} = \frac{1}{2}\gamma_{yz} \tag{2}$$

where **e** is the membrane strain in the mean surface, $\boldsymbol{\chi}$ is the curvature and **Γ** is the transverse shear strain [33,34].

$$\boldsymbol{\chi} = \begin{bmatrix} \chi_{xx} \\ \chi_{yy} \\ \chi_{xy} \end{bmatrix} = \begin{bmatrix} \dfrac{\partial \theta_y}{\partial x} \\ -\dfrac{\partial \theta_x}{\partial y} \\ \dfrac{\partial \theta_y}{\partial y} - \dfrac{\partial \theta_x}{\partial x} \end{bmatrix} \qquad \boldsymbol{\Gamma} = \begin{bmatrix} \gamma_{xz} \\ \gamma_{yz} \end{bmatrix} = \begin{bmatrix} \theta_y + \dfrac{\partial w}{\partial x} \\ -\theta_x + \dfrac{\partial w}{\partial y} \end{bmatrix} \tag{3}$$

If the transverse shear strain is zero or very low, which is often verified when the plate is very thin, then $\boldsymbol{\Gamma} = 0$. The Kirchhoff theory is thus obtained where the directions initially perpendicular to the middle surface remain perpendicular to the deformed middle surface.

These plate approaches are very efficient for the analysis of thin structures because the kinematics of the deformation is given by a reduced number of variables $(\overline{u}, \overline{v}, \overline{w}, \theta_x, \theta_y)$ that are function of (x,y). Nevertheless, in order to use them, it is necessary that the kinematic hypothesis on which they are based is verified. It will be seen that this is not the case for fibrous reinforcements.

Fig. 1 shows examples of deformation of composite fibre reinforcements. It can be seen from all the examples that the material normals (direction initially perpendicular to the middle surface and fixed to the material) do not remain perpendicular to the middle surface of the textile reinforcement. The deformations do not correspond to Kirchhoff's theory. The angle between the material normals and the middle surface is often very different from 90°. The deformation of the fibrous reinforcements has two main features. The fibres of which they are composed (carbon fibres in the examples in Fig. 1) are almost inextensible. Especially during a forming process, the fibres practically do not elongate. Besides, some slippage may occur between the fibres. These two aspects form the physical basis for the deformation of these materials and are specific to textile reinforcements. They are the basis of the proposed specific shell approach.

Kirchhoff's hypothesis (the material normal remains perpendicular to the middle surface) which reflects the physics of the deformation of standard materials, in particular when they are thin, is abandoned here and replaced by the constraint of inextensibility of the fibres. The Mindlin approach, by the transverse shear **Γ** (Eq. (3)) makes it possible that the material normal does not remain necessarily perpendicular to the middle surface. In Mindlin's model, the transverse shear strain is defined by a constitutive law that relates it to the shear stress [33–35]. This does not correspond to the physics of fibre reinforcement deformation. The position of the material normals after deformation is defined by the quasi inextensibility of the fibres and the possibility of slippage between them. Fig. 1c and d shows the deformation of a textile reinforcement composed of 11 layers of carbon reinforcement G1151 (Hexcel). Fig. 1c shows the experimental deformation where the material normals were marked and Fig. 1d shows the simulation performed using the Mindlin S3 shell finite element of Abaqus software. The tensile and transverse shear properties have been optimized so that the middle surface is in agreement with the experiment. However, the material normals obtained by simulation do not correspond to the experiment. Furthermore, an example of bending of thin textile reinforcement (Fig. 1e) shows that the normals do not tend to be perpendicular to the middle surface after deformation when the thickness is small. Unlike Mindlin shells, textile reinforcements do not tend towards Kirchhoff's theory when the thickness is small.

The objective of the present work is to develop a 3D shell approach that is tailored to the deformation physics of the fibre reinforcements. The objective of this shell approach is to determine all the kinematics and stresses in the entire thickness of the textile reinforcement. It is an alternative to the 3D finite element approaches (solid elements) that have been developed for this purpose [36–39] but with a better numerical efficiency, the number of degrees of freedom being much lower.

Therefore, a continuum mechanics-based 3D shell element is developed. The kinematics associated with the form of the virtual work taken into account reflect the specificity of the deformation modes of the fibre reinforcements (quasi inextensibility of the fibres and the possibility of slippage between fibres). Examples of 3D deformation of textile reinforcements are analysed both experimentally and simulated with good agreement using the proposed approach.

The fibre reinforcements under consideration are composed of two

directions of quasi inextensible fibres. This is an idealized situation. In practice, woven composite fibre reinforcements and their stacking are close to this situation. The weaving creates a crimp and the condition of inextensibility is not strictly observed. Nevertheless, on the one hand the geometries of the textile reinforcements are very flat in order to give good mechanical characteristics to the composite, on the other hand, during a process, the deformations of the reinforcement are large and the stresses are moderate. Consequently, in practice, for these composite woven reinforcements, the condition of inextensibility is a correct assumption. This can be verified in all the tests presented in this article, in particular Fig. 1.

3. Continuum mechanics-based 3D shell element for fibrous reinforcement

3.1. Geometry of the 3D shell element

The proposed shell is developed within the framework of continuum-based shell elements which was widely used to define effective shell elements [30–32]. In this article, this fibrous triangular shell element possesses 3 nodes, the geometry is shown in Fig. 2, the position vector of a point $M(\xi,\eta,\zeta)$ is defined as:

$$\boldsymbol{x}(M) = \boldsymbol{x}(H) + \boldsymbol{y}(M) \tag{4}$$

H is a point defined at the middle surface. ξ,η,ζ are the element natural coordinates (Fig. 2) with $0\leqslant\xi\leqslant1$, $0\leqslant\eta\leqslant1$, $-1\leqslant\zeta\leqslant1$. The coordinates ξ,η give the in-plane position. The element edges coincide with warp and weft directions, ζ is along the material normal direction which joints the top-bottom layer.

The position interpolation in the element is given by:

$$\boldsymbol{x}(\xi,\eta,\zeta) = \sum_{k=1}^{3} N_k \boldsymbol{x}_k + \sum_{k=1}^{3} N_k \frac{\zeta}{2} h_m^k \boldsymbol{V}_m^k \tag{5}$$

where $\mathbf{x}_k$ is the position vector of node k, h_m^k is the thickness along the direction of material director $\mathbf{V}_m^k$ which is the unit material director defined at each node k. N_k is the shape function at node k.

$$N_1 = 1-\xi-\eta; \quad N_2 = \xi; \quad N_3 = \eta \tag{6}$$

A local orthogonal frame $(\boldsymbol{V}_1^k, \boldsymbol{V}_2^k, \boldsymbol{V}_3^k)$ is defined at each node k(Fig. 2). $\boldsymbol{e}_1,\boldsymbol{e}_2,\boldsymbol{e}_3$ is the global unit base vector, $\mathbf{n}$ is the unit vector normal to the element's mid-surface.

$$\boldsymbol{V}_3^k = \boldsymbol{V}_m^k, \ \mathbf{V}_1^k = \frac{\boldsymbol{e}_2 \times \boldsymbol{V}_3^k}{\left|\boldsymbol{e}_2 \times \boldsymbol{V}_3^k\right|}, \ \boldsymbol{V}_2^k = \boldsymbol{V}_3^k \times \boldsymbol{V}_1^k \tag{7}$$

A point with position $\mathbf{x}$ in the element gives the covariant vectors with respect to natural coordinates:

$$\mathbf{g}_1 = \frac{\partial \mathbf{x}}{\partial \xi}, \ \mathbf{g}_2 = \frac{\partial \mathbf{x}}{\partial \eta}, \ \mathbf{g}_3 = \frac{\partial \mathbf{x}}{\partial \zeta} \tag{8}$$

In order to avoid locking due to fibre inextensibility, the vector along the direction of the warp and weft fibres $\mathbf{k}_1, \mathbf{k}_2$ are equal to the covariant vectors $\mathbf{g}_1, \mathbf{g}_2$ [40,41].

$$\mathbf{g}_1 = \mathbf{k}_1, \ \mathbf{g}_2 = \mathbf{k}_2 \tag{9}$$

3.2. Conservation of the thickness in the direction of the normal

As in the classic shell models, the approach presented is for cases where there are no external forces in the thickness direction or where these are not taken into account. The thickness of the reinforcement in the direction of the normal to its mean surface is the sum of the thicknesses of the fibres which are assumed to be in contact. This thickness in the direction of the normal remains constant during deformation. It can be seen, especially in Fig. 1, that this hypothesis is verified in the experiments. This assumption complete the kinematics. Consequently:

$$h_m^k = \frac{h}{\mathbf{V}_m^k \cdot \mathbf{n}} \tag{10}$$

where h is the thickness along the direction normal to the mid-surface of the shell, h_m^k is the thickness along the material director $\mathbf{V}_m^k$ at node k.

3.3. Kinematics of the fibrous shell

By considering the kinematic equation of continuum-based element, the expression of the incremental displacement for each point in the element between the geometry at time ${}^{i}t$ and ${}^{i+1}t$ is developed:

$$\Delta\boldsymbol{u}(\xi,\eta,\zeta) = {}^{i+1}\boldsymbol{x} - {}^{i}\boldsymbol{x} \tag{11}$$

Taking Eq. (5) into account:

$$\begin{aligned}\Delta\boldsymbol{u}(\xi,\eta,\zeta) &= \sum_{k=1}^{3} N_k ({}^{i+1}\boldsymbol{x}_k - {}^{i}\boldsymbol{x}_k) + \sum_{k=1}^{3} N_k \frac{\zeta}{2} ({}^{i+1}h_m^k \, {}^{i+1}\boldsymbol{V}_m^k - {}^{i}h_m^k \, {}^{i}\boldsymbol{V}_m^k) \\ &= \sum_{k=1}^{3} N_k \Delta\boldsymbol{u}_k + \sum_{k=1}^{3} N_k \frac{\zeta}{2} ({}^{i+1}h_m^k \, {}^{i+1}\boldsymbol{V}_m^k - {}^{i}h_m^k \, {}^{i}\boldsymbol{V}_m^k)\end{aligned} \tag{12}$$

The rotation of material director is given by two rotation components α and β. On the time step from ${}^{i}t$ to ${}^{i+1}t$:

$${}^{i+1}\mathbf{V}_m^k - {}^{i}\mathbf{V}_m^k = \Delta\alpha_k \, {}^{i}\mathbf{V}_1^k - \Delta\beta_k \, {}^{i}\mathbf{V}_2^k \tag{13}$$

The update of thickness along material director direction is:

$$\Delta h_m^k = {}^{i+1}h_m^k - {}^{i}h_m^k = \frac{h}{{}^{i+1}\mathbf{n}({}^{t}\mathbf{V}_m^k + \Delta\alpha_k \, {}^{i}\mathbf{V}_1^k - \Delta\beta_k \, {}^{i}\mathbf{V}_2^k)} - \frac{h}{{}^{i}\mathbf{n} \, {}^{i}\mathbf{V}_m^k} \tag{14}$$

where the expression of the updated unit normal vector ${}^{i+1}\mathbf{n}$ is.

$${}^{i+1}\boldsymbol{n} = \frac{{}^{i+1}\boldsymbol{g}_1 \times {}^{i+1}\boldsymbol{g}_2}{\| {}^{i+1}\boldsymbol{g}_1 \times {}^{i+1}\boldsymbol{g}_2 \|} = \frac{({}^{i}\boldsymbol{g}_1 + \Delta\boldsymbol{u}_2 - \Delta\boldsymbol{u}_1) \times ({}^{i}\boldsymbol{g}_2 + \Delta\boldsymbol{u}_3 - \Delta\boldsymbol{u}_1)}{\| ({}^{i}\boldsymbol{g}_1 + \Delta\boldsymbol{u}_2 - \Delta\boldsymbol{u}_1) \times ({}^{i}\boldsymbol{g}_2 + \Delta\boldsymbol{u}_3 - \Delta\boldsymbol{u}_1) \|} \tag{15}$$

Taking Eqs. (13)–(15) into Eq. (12), the displacement increment is:

v

$$\Delta\boldsymbol{u}(\xi,\eta,\zeta) = \sum_{k=1}^{3} N_k \Delta\boldsymbol{u}_k + \sum_{k=1}^{3} N_k \frac{\zeta}{2} ({}^{i}h_m^k + \Delta h_m^k)(\Delta\alpha_k \, {}^{i}\boldsymbol{V}_1^k - \Delta\beta_k \, {}^{i}\boldsymbol{V}_2^k) + \sum_{k=1}^{3} N_k \frac{\zeta}{2} \Delta h_m^k \, {}^{i}\boldsymbol{V}_m^k \tag{16}$$

The above formulation results in five degrees of freedom per node. $\Delta\boldsymbol{u}_k$ is the nodal incremental translation displacement vector, the other two DOFs are two rotations components. The configuration at ${}^{i+1}t$ enable the calculation of the internal nodal loads at ${}^{i+1}t$.

4. Internal virtual work of the textile reinforcement

For any virtual displacement equal to zero on the boundary with prescribed displacement, the virtual work theory is written:

$$\delta W_{\text{ext}} - \delta W_{int} = \delta W_{\text{acc}} \tag{17}$$

The internal virtual work is separated into three parts:

$$\delta W_{int} = \delta W_{int}^{Ten} + \delta W_{int}^{Bend} + \delta W_{int}^{Shear} \tag{18}$$

In Eq. (18), δW_{int} denotes internal virtual work, δW_{int}^{Ten}, δW_{int}^{Bend}, δW_{int}^{Shear} are the tension, bending, in-plane shear internal virtual works respectively.

$$\delta W_{int}^{Ten} = \sum_{f=1}^{Nfibres} \int_{Lf} T^{11f}\ \delta\varepsilon_{11}^{f}\ dL + \sum_{f=1}^{Nfibres} \int_{Lf} T^{22f}\ \delta\varepsilon_{22}^{f}\ dL \tag{19}$$

$$\delta W_{int}^{Bend} = \sum_{f=1}^{Nfibres} \int_{Lf} M^{11f}\ \delta\chi_{11}^{f}\ dL + \sum_{f=1}^{Nfibres} \int_{Lf} M^{22f}\ \delta\chi_{22}^{f}\ dL \tag{20}$$

$$\delta W_{int}^{Shear} = \sum_{f=1}^{Nfibres} \int_{\Omega} M^{sf}\ \delta\gamma^{f}\ d\Omega \tag{21}$$

The superscript f indicates the fibre in consideration. T^{11}, T^{22} are the tensions in the fibres in the warp and weft direction, $\delta\varepsilon_{11}$,$\delta\varepsilon_{22}$ are virtual tensile strains; M^{11},M^{22} are the bending moment on the fibres in warp and weft directions, $\delta\chi_{11}$,$\delta\chi_{22}$ are the virtual curvature; M^{s} is the in-plane shear moment, $\delta\gamma$ is the virtual in-plane shear angle.

The form (Eqs. (19)–(21)) of the internal virtual work corresponds to the specific mechanical behaviour of the fibrous reinforcements. The virtual tension work takes into account the high tensile rigidity of the fibres and leads to the quasi-inextensibility of the fibres. It controls the deformation of the fibrous medium. The quasi-inextensibility of the fibres at different altitudes in the thickness of the reinforcement leads to specific positions of the normals as shown in the different examples (e.g. Fig. 1). The virtual bending work considers the bending stiffness of each fibre. It will also be shown in Section 5.2 that it makes it possible to take into account the friction between the fibres for certain materials. The in-plane shear stiffness in the plane is taken into account in a standard manner for textiles [42–46]. No other stiffness is taken into account thus making it possible for the fibres to slip between the fibres whereas it is not possible in a standard shell approach.

Although most forming processes are quasi-static, the simulation is often based on an explicit dynamic approach. [47–49]. The principle of virtual work and the finite element approximation leads to:

$$\mathbf{M}\ddot{\mathbf{u}} + \mathbf{C}\dot{\mathbf{u}} = \mathbf{F}_{\text{ext}} - \mathbf{F}_{\text{int}} \tag{22}$$

$\mathbf{M}$ and $\mathbf{C}$ are the mass and damping matrices respectively. $\mathbf{F}_{int}$ and $\mathbf{F}_{\text{ext}}$ are the internal and exterior nodal loads. $\mathbf{F}_{int}$ is specific to the textile reinforcements and is composed of three parts: the tensile nodal loads $\mathbf{F}_{int}^{\text{Ten}}$, the bending nodal loads $\mathbf{F}_{int}^{\text{Bend}}$ and the in-plane shear nodal loads $\mathbf{F}_{int}^{\text{Shear}}$. The calculation of $\mathbf{F}_{int}$ for the specific form of virtual works given in Eqs. (17)–(19) is a main point of the approach presented and is the subject of Section 4.1 below.

The central difference scheme on a time step ${}^{i}\Delta t = {}^{i+1}t - {}^{i}t$ gives the nodal displacement increment:

$${}^{i+1}\mathbf{u}_N = {}^{i}\mathbf{u}_N + ({}^{i-1/2}\dot{\mathbf{u}}_N + \frac{1}{2}({}^{i-1}\Delta t + {}^{i}\Delta t)\mathbf{M}^{-1}({}^{i}\mathbf{F}_{ext} - {}^{i}\mathbf{F}_{int}))\,{}^{i}\Delta t \tag{23}$$

$\mathbf{M}$ is the lumped matrix for node k of the shell. It is given in appendix A [50].

4.1. Calculation of internal nodal force

4.1.1. Tension

The nodal tensile internal loads $\mathbf{F}_{int}^{\text{Ten}}$ for the element consists of two parts. The first part denoted by $\mathbf{F}^{\text{Ten}}$ concerns the displacement degrees of freedom. The second part denoted by $\mathbf{M}^{\text{Ten}}$ concerns the rotation degrees of freedom.

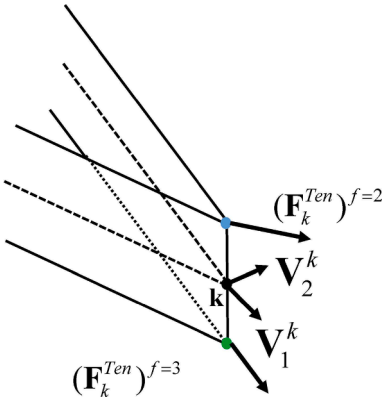

Fig. 3. Moment produced by internal force at top-bottom position of node k. (For interpretation of the references to colour in this figure legend, the reader is referred to the web version of this article.)

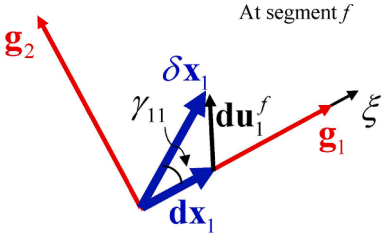

Fig. 4. In-plane shear angle and virtual displacement. (For interpretation of the references to colour in this figure legend, the reader is referred to the web version of this article.)

$$\mathbf{F}^{\text{Ten}} = \sum_{f=1}^{n} \int_{Lf} (\mathbf{B}_{11}^{Ten})^{f^T} T^{11f} dL + \sum_{f=1}^{n} \int_{Lf} (\mathbf{B}_{22}^{Ten})^{f^T} T^{22f} dL \tag{24}$$

Here $(\mathbf{B}_{\alpha\alpha}^{Ten})^{f}$ matrix is the fibre tension strain interpolation matrix, in which the right subscript $\alpha\alpha$ represent the component in different fibre directions, α takes value 1 or 2. n is the number of fibres in the thickness considered for numerical integration. In the present work $n = 3$. The tensile virtual strain in direction α for the fibre f is consequently:

$$(\delta\varepsilon_{\alpha\alpha})^{f} = (\mathbf{B}_{\alpha\alpha}^{Ten})^{f}\,\delta\mathbf{u}^{f} \tag{25}$$

$\mathbf{u}^{f}$ is the single column displacement matrix for fibre end points of the segment f. It is obtained from nodal displacements and rotations matrix $\mathbf{u}$ by using Eq. (16). With the Eq. (9), assigning the fibre direction as the direction of element edge, the virtual strain is shown (Eq. (26)) with

$$\xi^1 = \xi \ ;\ \xi^2 = \eta \ ;\ \xi^3 = \zeta$$

$$(\delta\varepsilon_{\alpha\alpha})^{f} = \frac{\mathbf{g}_{\alpha}^{f}}{\left\|\mathbf{g}_{\alpha}^{f}\right\|^2} \cdot \left\langle \frac{\partial N_1(\xi,\eta)}{\partial\xi^{\alpha}} \quad \frac{\partial N_2(\xi,\eta)}{\partial\xi^{\alpha}} \quad \frac{\partial N_3(\xi,\eta)}{\partial\xi^{\alpha}} \right\rangle \begin{Bmatrix} \delta\mathbf{u}_1^{f} \\ \delta\mathbf{u}_2^{f} \\ \delta\mathbf{u}_3^{f} \end{Bmatrix} \tag{26}$$

The $(\mathbf{B}_{\alpha\alpha}^{Ten})^{f}$ is given as:

$$(\mathbf{B}_{\alpha\alpha}^{Ten})^{f} = \frac{\mathbf{g}_{\alpha}^{f}}{\left\|\mathbf{g}_{\alpha}^{f}\right\|^2} \cdot \left\langle \frac{\partial N_1(\xi,\eta)}{\partial\xi^{\alpha}} \quad \frac{\partial N_2(\xi,\eta)}{\partial\xi^{\alpha}} \quad \frac{\partial N_3(\xi,\eta)}{\partial\xi^{\alpha}} \right\rangle \tag{27}$$

The second part is the load provided by the force at top and bottom fibre (Fig. 3). The tensile force in the different fibres in the thickness generate moments at node k:

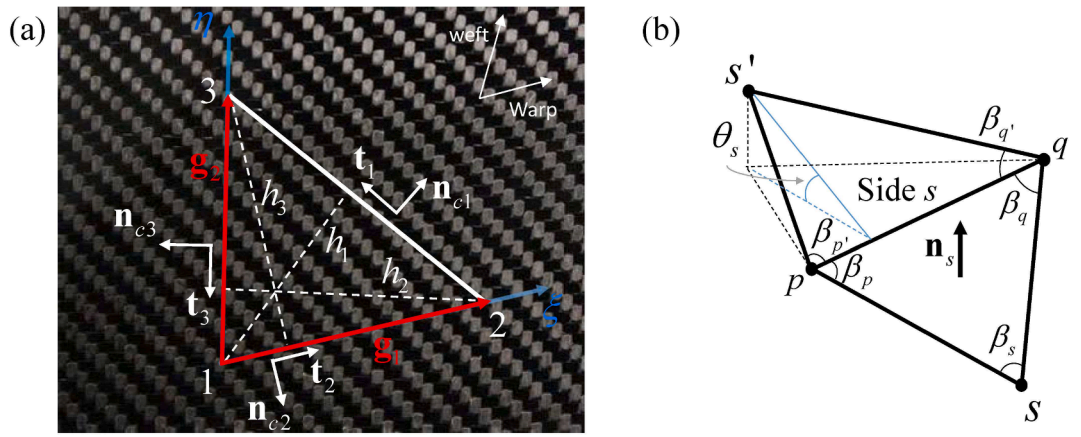

Fig. 5. (a) Triangular element mid-surface (b) Parameters defined in two neighbouring elements. (For interpretation of the references to colour in this figure legend, the reader is referred to the web version of this article.)

$$M^{Ten}_{\alpha\_k} = \sum_{f=1}^{n} \frac{\zeta h^k_m}{2}\left(\left(\mathbf{F}^{Ten}_k\right)^f \cdot \mathbf{V}^k_1\right), \qquad M^{Ten}_{\beta\_k} = -\sum_{f=1}^{n} \frac{\zeta h^k_m}{2}\left(\left(\mathbf{F}^{Ten}_k\right)^f \cdot \mathbf{V}^k_2\right) \tag{28}$$

$$\mathbf{M}^{Ten} = \left[M^{Ten}_{\alpha} \; M^{Ten}_{\beta}\right] \tag{29}$$

Eq. (28) shows the two nodal moment components corresponding with rotations α, β. The tensile internal load is obtained by assembling two parts $\mathbf{F}^{Ten}$ and $\mathbf{M}^{Ten}$.

4.1.2. In-plane shear

The shear angle γ^f for the element at position f is:

$$\delta\gamma^f = \left(\mathbf{B}^{Shear}\right)^f \delta\mathbf{u}^f \tag{30}$$

In Fig. 4, considering the fibre in direction $\alpha = 1$ for example, the angle between $d\mathbf{x}_1$ and $\delta\mathbf{x}_1$ is denoted by γ_{11}. Consequently γ_{22} will represent the angle between $d\mathbf{x}_2$ and $\delta\mathbf{x}_2$. The virtual angle between warp and weft direction is given as the combination of these two angles [25] in form of Eq. (31) which gives $\left(\mathbf{B}^{Shear}\right)^f$:

$$\delta\gamma^f = \left(\frac{\partial \mathbf{u}^f}{\partial\xi}\cdot\mathbf{k}_1\right)\frac{\mathbf{k}^2\cdot\mathbf{k}^1}{\|\mathbf{k}^2\|\|\mathbf{k}_1\|} + \left(\frac{\partial \mathbf{u}^f}{\partial\eta}\cdot\mathbf{k}_1\right)\frac{\|\mathbf{k}^2\|}{\|\mathbf{k}_1\|} - \left(\frac{\partial \mathbf{u}^f}{\partial\eta}\cdot\mathbf{k}_2\right)\frac{\mathbf{k}^1\cdot\mathbf{k}^2}{\|\mathbf{k}^1\|\|\mathbf{k}_2\|} - \left(\frac{\partial \mathbf{u}^f}{\partial\xi}\cdot\mathbf{k}_2\right)\frac{\|\mathbf{k}^1\|}{\|\mathbf{k}_2\|} \tag{31}$$

By using the same method as described in Section 4.1.1 for tension, the internal loads $\mathbf{F}^{Shear}_{int}$ will also be divided into two parts, and they could be calculated from matrix $\left(\mathbf{B}^{Shear}\right)^f$ and the thickness along

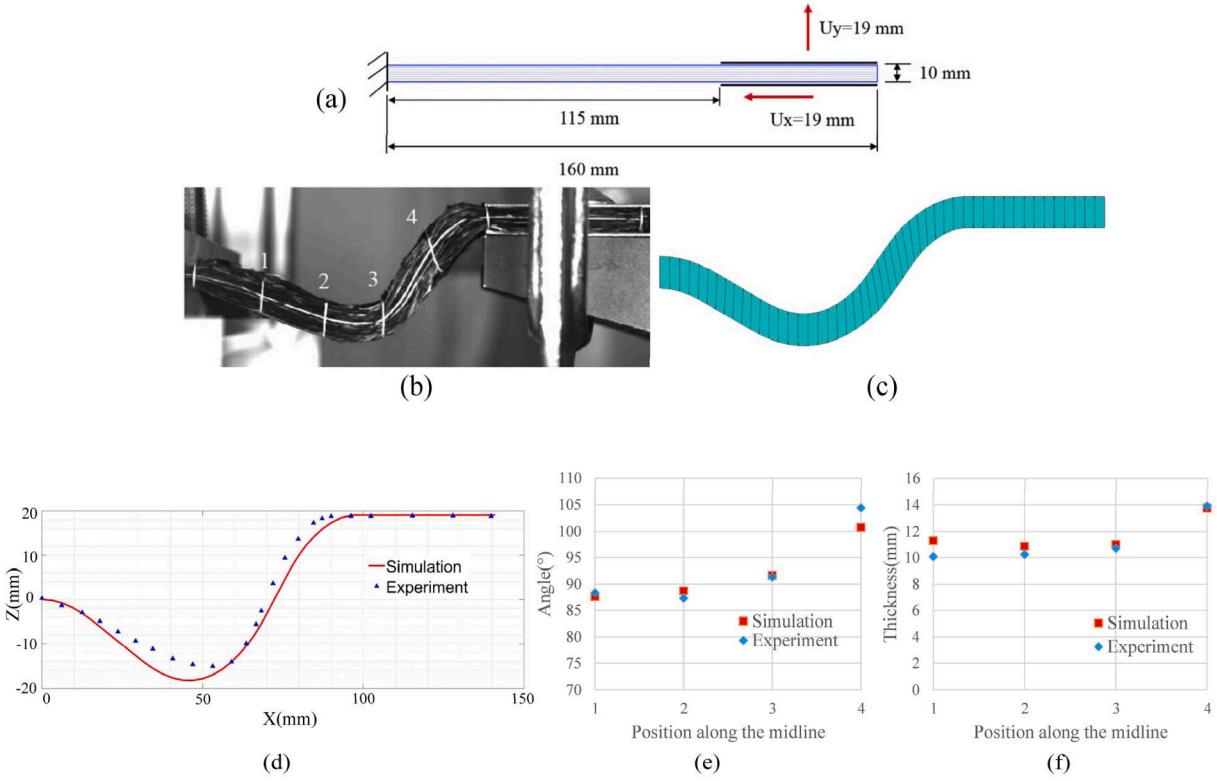

Fig. 6. Bending test on a multilayer textile reinforcement (a) Test condition (b) Experiment (c) Simulation by 3D shell element. (d) Position of mid-surface. (e) Angles between material directors and horizontal direction. (f) Thickness along material director. (For interpretation of the references to colour in this figure legend, the reader is referred to the web version of this article.)

Table 1
Mechanical properties of single layer in multilayer reinforcement (Section 5.1).

Tension stiffness (per unit width)	1200 N/mm
Bending stiffness (per unit width)	B = 7.5 N·mm when $\lvert\chi_{\alpha\alpha}\rvert \leqslant 0.001$ With $M^{\alpha\alpha} = B\chi_{\alpha\alpha}$ 0.5 N·mm when $\chi_{\alpha\alpha} \geqslant 0.001$ With $M^{\alpha\alpha} = B\chi_{\alpha\alpha} + 0.0075$ 0.5 N·mm when $\chi_{\alpha\alpha} \leqslant -0.001$ With $M^{\alpha\alpha} = B\chi_{\alpha\alpha} - 0.0075$

material director.

$$\mathbf{F}^{\text{Shear}} = \sum_{f=1}^{n} \left(\mathbf{B}^{Shear}\right)^{f^T} \left(C_\gamma\right)^f \tag{32}$$

The moment produced by force $\left(\mathbf{F}^{\text{Shear}}\right)^f$ at different position in the thickness is:

$$M_{\alpha\_k}^{\text{Shear}} = \sum_{f=1}^{n} \frac{\zeta h_m^k}{2} \left(\left(\mathbf{F}_k^{\text{Shear}}\right)^f \cdot \mathbf{V}_1^k\right) \qquad M_{\beta\_k}^{\text{Shear}} = -\sum_{f=1}^{n} \frac{\zeta h_m^k}{2} \left(\left(\mathbf{F}_k^{\text{Shear}}\right)^f \cdot \mathbf{V}_2^k\right) \tag{33}$$

The internal in-plane shear nodal internal loads are $\mathbf{F}^{\text{Shear}}$, $\mathbf{M}^{\text{Shear}}$.

4.1.3. Bending

The curvature is calculated from the position of the neighbouring elements. This method has been developed to obtain rotation free shell element [51–53].

The virtual curvature in warp and weft direction is interpolated from the nodal virtual displacement:

$$\delta\chi_{\alpha\alpha} = \mathbf{B}_{\alpha\alpha}^{Bend} \delta\mathbf{u} \tag{34}$$

Fig. 5 shows some parameters defined in the element. The height from node k is denoted as h_k, $\mathbf{n}_c$ is the exterior normal to side in the element's plane, the relative rotation angle between the principal element plane and neighbour element around the side s is denoted by θ_s, s vary in (1,2,3), s' is the corresponding node number in neighbour element. Denoting $\widehat{\mathbf{g}}_\alpha$ the unit vector of $\mathbf{g}_\alpha$, the curvature in the fibre direction is obtained [25]:

$$\chi_{\alpha\alpha} = -\sum_{s=1}^{3} \left(\frac{2(\widehat{\mathbf{g}}_\alpha \mathbf{n}_{cs})^2}{h_s} \quad \frac{h_s \theta_s}{h_s + h_{s'}} \right) \quad \text{with } \delta\theta_s = \delta\varphi_{s'} + \delta\varphi_s \tag{35}$$

φ_s and $\varphi_{s'}$ are respectively the rotation angle of the principal element and the neighbour element around side s. They are represented by the incremental nodal displacements where p and q are the complements of s in (1,2,3): (Fig. 5)

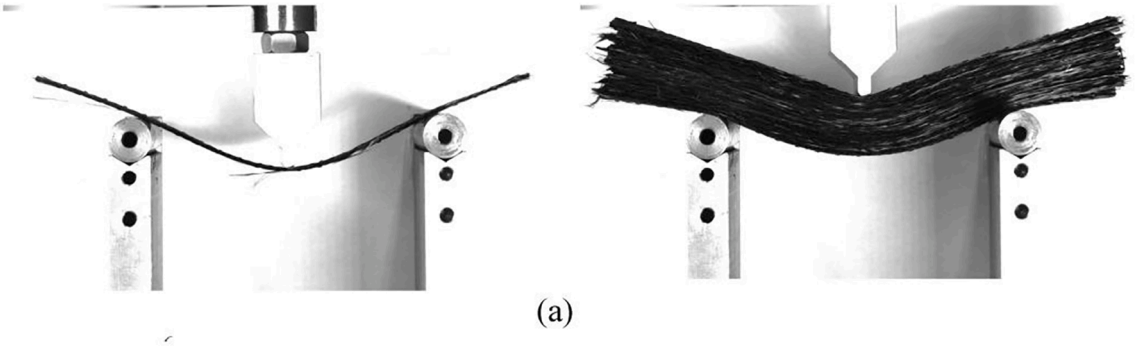

(a)

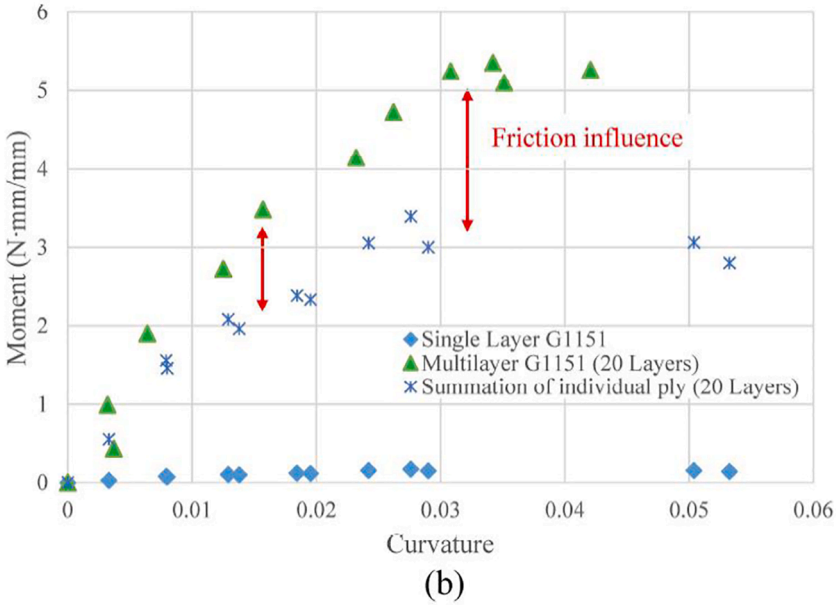

(b)

Fig. 7. (a) 3-Points bending test on a single ply and twenty plies of Hexcel G1151 (b) Moment-curvature data for multilayer reinforcement. (For interpretation of the references to colour in this figure legend, the reader is referred to the web version of this article.)

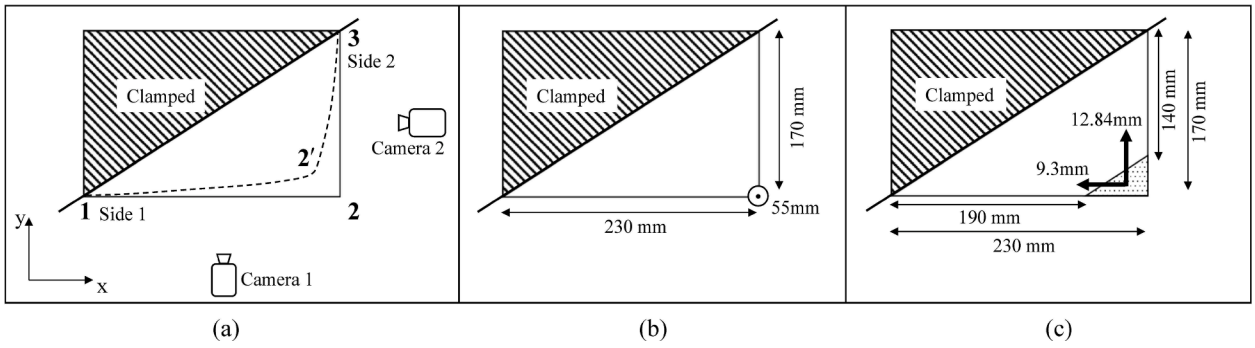

Fig. 8. (a) Schema of 3D experiment (b) Boundary condition of Test 6.1.1 (c) Boundary condition of Test 6.1.2. (For interpretation of the references to colour in this figure legend, the reader is referred to the web version of this article.)

$$\delta\varphi_s = \frac{\delta\mathbf{u}_s\cdot\mathbf{n}_s}{h_s} - \frac{cos\beta_q}{h_p}\delta\mathbf{u}_p\cdot\mathbf{n}_s - \frac{cos\beta_p}{h_q}\delta\mathbf{u}_q\cdot\mathbf{n}_s \tag{36}$$

Thus θ_s can be given by the nodal displacements $\delta\mathbf{u}$, this gives the bending strain interpolation matrix $\mathbf{B}_{\alpha\alpha}^{Bend}$, consequently, the nodal bending internal loads are:

$$\mathbf{F}_{int}^{\text{Bend}} = \int_L (\mathbf{B}_{11}^{Bend})^T M^{11} dL + \int_L (\mathbf{B}_{22}^{Bend})^T M^{22} dL \tag{37}$$

$M^{\alpha\alpha}$ is a function of the curvature measured in bending experiment [54]. The detail of the calculation of the bending nodal internal loads can be found in [25,52].

5. Numerical simulations and experimental comparisons in 2D

5.1. Bending test on a multilayer textile reinforcement

The specimen consists of 20 plies of Hexcel G986® carbon twill weave stacked in the same orientation (Fig. 6). The horizontal and vertical displacements are imposed at the right end of specimen, meanwhile the other is clamped. The experimental deformed shape is shown in Fig. 6b. The simulation based on the proposed shell element is shown in Fig. 6c. The material properties of Hexcel G986 are given in Table 1 [55]. Comparisons between numerical and experimental results is given in Fig. 6d, e and f. The deflection, the rotation of the material director and the change in thickness along material director are in good agreement with experiment.

Furthermore, some other tests like cantilever bending test, have also been carried out and simulated by the 2D approach presented in [29] with a good agreement between tests and simulations. The 3D shell approach proposed in this paper leads to strictly identical results in these cases.

5.2. Influence of friction between fibres

In the approach proposed above in Sections 3 and 4, friction does not appear explicitly. Nevertheless, the friction between the fibres exists and has an influence that may not be negligible [56–58]. In order to highlight the influence of friction on bending stiffness, 3-point bending tests are carried out Fig. 7 on two specimens consisting of a single carbon fabric layer (Hexcel G1151®), and twenty layers of the same reinforcement respectively.

The measured bending moment versus curvature is shown in Fig. 7b. The measured bending stiffness of the stack made of twenty G1151 layers is larger than the summation of the bending rigidities of twenty individual fabrics. This difference is due to friction between the plies and is far from negligible. In order to take friction into account in a simple way in the simulations, the bending stiffness taken into account in the proposed shell element is that of the overall stack (and not the sum of the stiffness of the individual plies or fibres). From the point of view of experimental identification, the measurement of the stiffness of the global stack is no more complex and sometimes simpler than that of each ply.

Friction within a woven reinforcement is a complex problem and depends on a number of factors, in particular the clamping forces applied during forming [59]. Nevertheless, the proposed shell approach

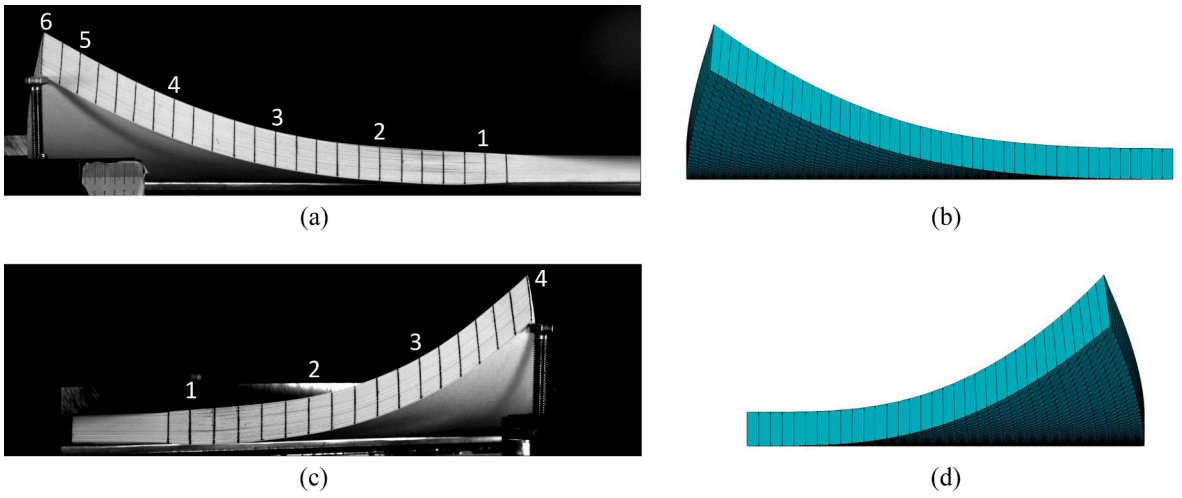

Fig. 9. Deformed shape along side 1. (a) Experiment. (b) Simulation. Deformed shape along side 2. (c) Experiment. (d) Simulation. (For interpretation of the references to colour in this figure legend, the reader is referred to the web version of this article.)

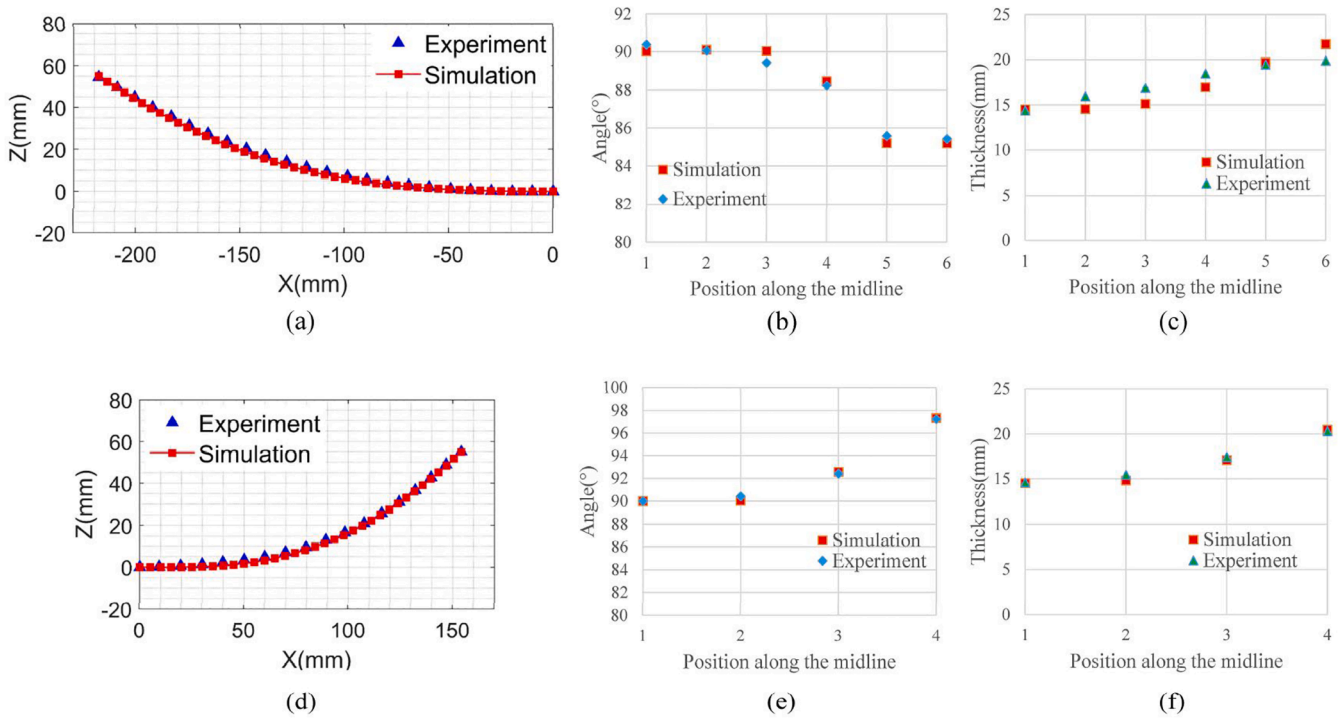

Fig. 10. (a) (d) Mid-surface along side 1 and side 2 (b) (e) Angles between the material directors and the horizontal direction along side 1 and side 2 (c) (f) Thickness along with material director along side 1 and side 2. (For interpretation of the references to colour in this figure legend, the reader is referred to the web version of this article.)

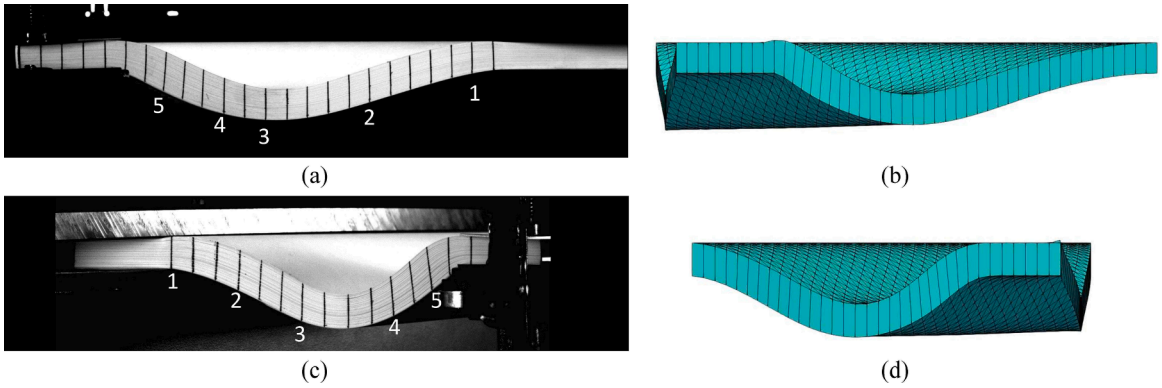

Fig. 11. Deformed shape along side 1. (a) Experiment (b) Simulation. Deformed shape along side 2. (c) Experiment (d) Simulation. (For interpretation of the references to colour in this figure legend, the reader is referred to the web version of this article.)

is macroscopic with only one element in the thickness of the reinforcement or reinforcement stack. The approach used to take into account the friction between the fibres makes it possible to remain within this framework and to be quite effective. Furthermore, measuring the bending stiffness of the reinforcement is quite simple. This approach has its limitations, especially in the case of complex boundary conditions during a process. In such cases, it may be necessary to consider 3D or mesoscopic modelling.

6. Numerical simulations and experimental comparisons in 3D

In this section, the proposed approach is applied to 3D deformation cases. The part above the diagonal 1–3 of a rectangular fibrous specimen is clamped and the lower part is subject to bending (Fig. 8). The deformation of the two sides are captured by two cameras (Figs. 8a and 9). Some straight lines are drawn on both two sides in the through-thickness direction, they are initially normal to the mid-surface. They show the material directors and their rotations.

6.1. Bending test of a fibrous specimen

The specimen is a stack of 130 sheets of paper. It is not exactly a textile composite reinforcement but a model material which, with regard to bending, corresponds to the problem under consideration. The in-plane shear stiffness is large and the sheets of paper do not deform in in-plane shear.

6.1.1. Bending due to an imposed displacement of a corner

A rigid support imposes a vertical displacement at the corner of the rectangle specimen (Figs. 8b and 9). The experimental deformed configuration of the two sides are shown in Fig. 9a and c and the results of the corresponding simulations using the proposed shell approach are displayed in Fig. 9b and d.

Fig. 10 compares the experimental and numerical deformed middle

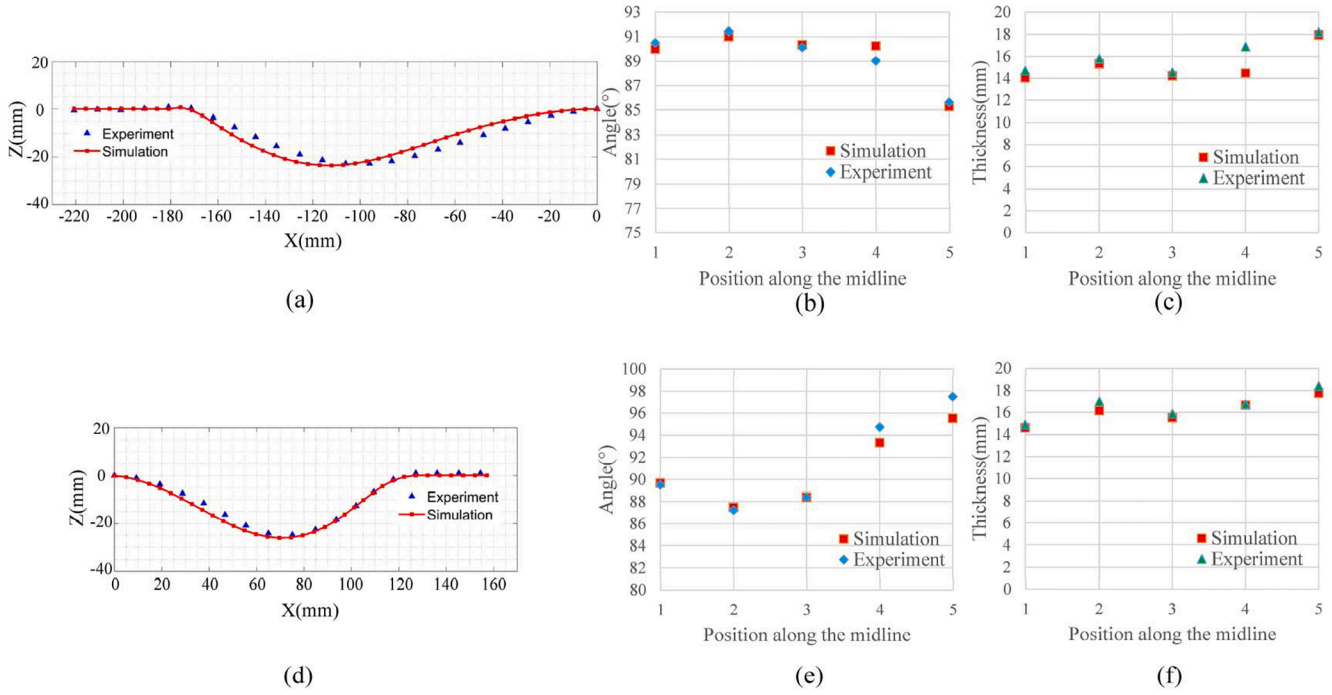

Fig. 12. (a) (d) Mid-surface along side 1 and side 2 (b) (e) Angles between the material directors and the horizontal direction along side 1 and side 2 (c) (f) Thickness along with material director along side 1 and side 2. (For interpretation of the references to colour in this figure legend, the reader is referred to the web version of this article.)

Table 2
Mechanical properties of G1151 multilayer reinforcement (Section 6.2).

Tension stiffness (per unit width)	2300 N/mm
Bending stiffness (per unit width)	Warp B = 72 N·mm Weft B = 68 N·mm

surface positions, material director rotation and thickness. The correspondence between the simulation and the experiment is pretty good. In this test, the curvature of the shell is non-zero and yet the material directors remain almost parallel. This is not in accordance with standard shell theory.

6.1.2. *Buckling bending test*

The diagonal of the specimen is clamped (Fig. 8). An in-plane displacement is imposed at the corner of the rectangle specimen (see

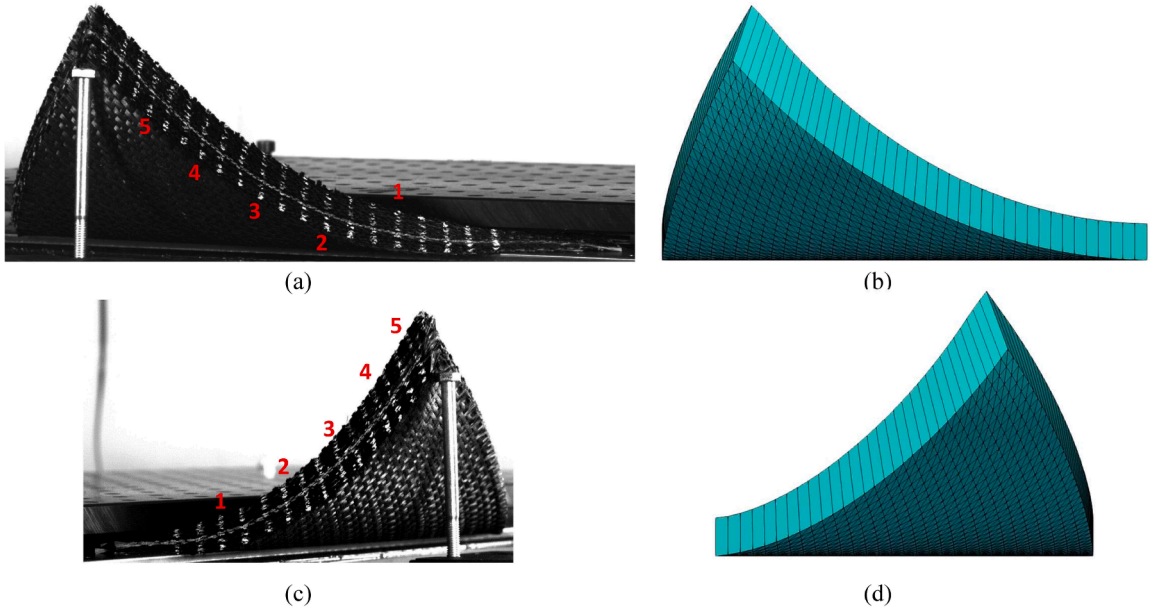

Fig. 13. Bending of a G1151 laminate due to an imposed displacement of a corner. Deformed shape along side 1. (a) Experiment. (b) Simulation. Deformed shape along side 2. (c) Experiment. (d) Simulation. (For interpretation of the references to colour in this figure legend, the reader is referred to the web version of this article.)

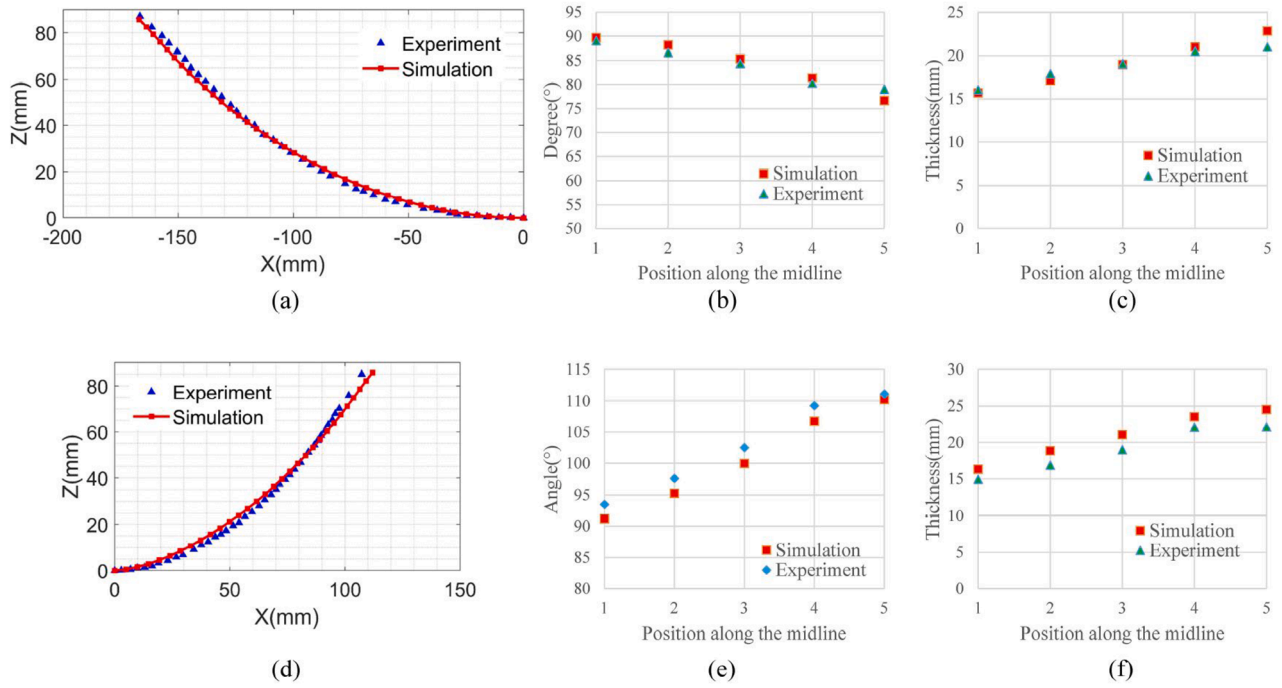

Fig. 14. Bending of a G1151 laminate due to an imposed displacement of a corner. (a) (d) Mid-surface along side 1 and side 2 (b) (e) Angles between the material directors and the horizontal direction along side 1 and side 2 (c) (f) Thickness along with material director along side 1 and side 2. (For interpretation of the references to colour in this figure legend, the reader is referred to the web version of this article.)

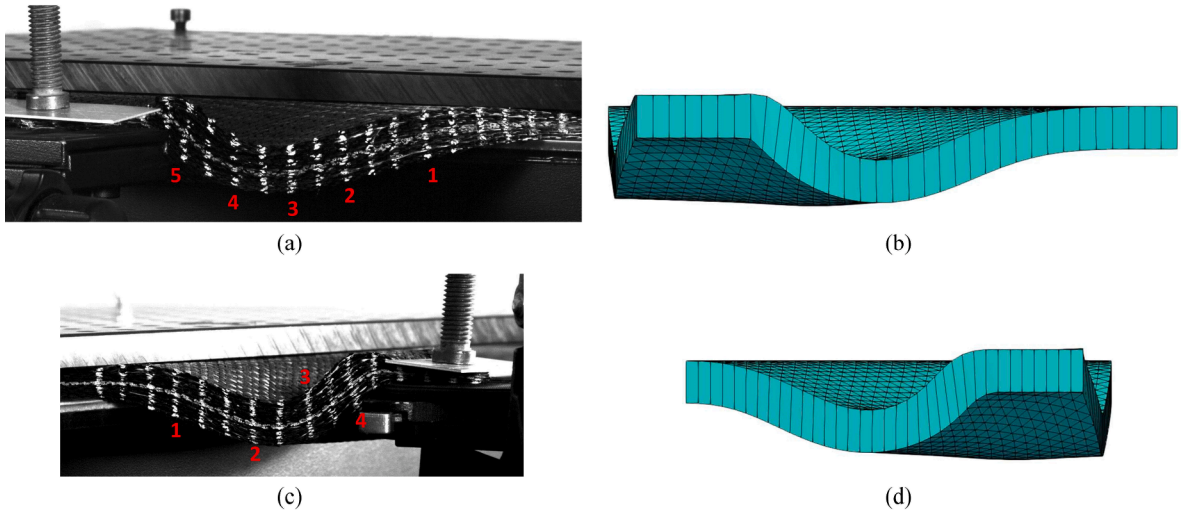

Fig. 15. Buckling bending test of a G1151 laminate. Deformed shape along side 1. (a) Experiment. (b) Simulation. Deformed shape along side 2. (c) Experiment. (d) Simulation. (For interpretation of the references to colour in this figure legend, the reader is referred to the web version of this article.)

Figs. 8c and 11). The deformed configuration is shown in Fig. 11. Fig. 12. compares the experimental and numerical deformed shapes with regard to mean surface position, material director rotation and thickness. The correspondence between the simulation and the experiment is pretty good.

6.2. *Bending of a carbon textile reinforcement*

The considered multilayer reinforcement is made up by 11 layers of G1151 carbon weaves. The dimension of the laminate is $200mm \times 150mm \times 15mm$. The mechanical properties of G1151 have been determined in several previous studies [60–62]. The bending stiffness of this multilayer specimen is measured in three point bending test, the influence of friction is taken into account (Table 2).

6.2.1. *Bending due to an imposed displacement of a corner*

The G1151 laminate reinforcement is subjected to an imposed displacement of a corner (Figs. 8b and 13). The experimental deformed configuration captured on two sides are shown in Fig. 13a and c, the corresponding simulation result is shown in Fig. 13b and d. The position of the mid-surface, the material director directions and thicknesses are shown in Fig. 14. The simulation shows a good agreement with experiment, which was not be obtained with the Abaqus S3 Mindlin shell element.

6.2.2. *Buckling bending test*

An in-plane displacement is imposed at the corner of the rectangle G1151 laminate reinforcement with a clamped diagonal (Figs. 8c and 15). The deformed configuration is shown in Fig. 15a and c, the

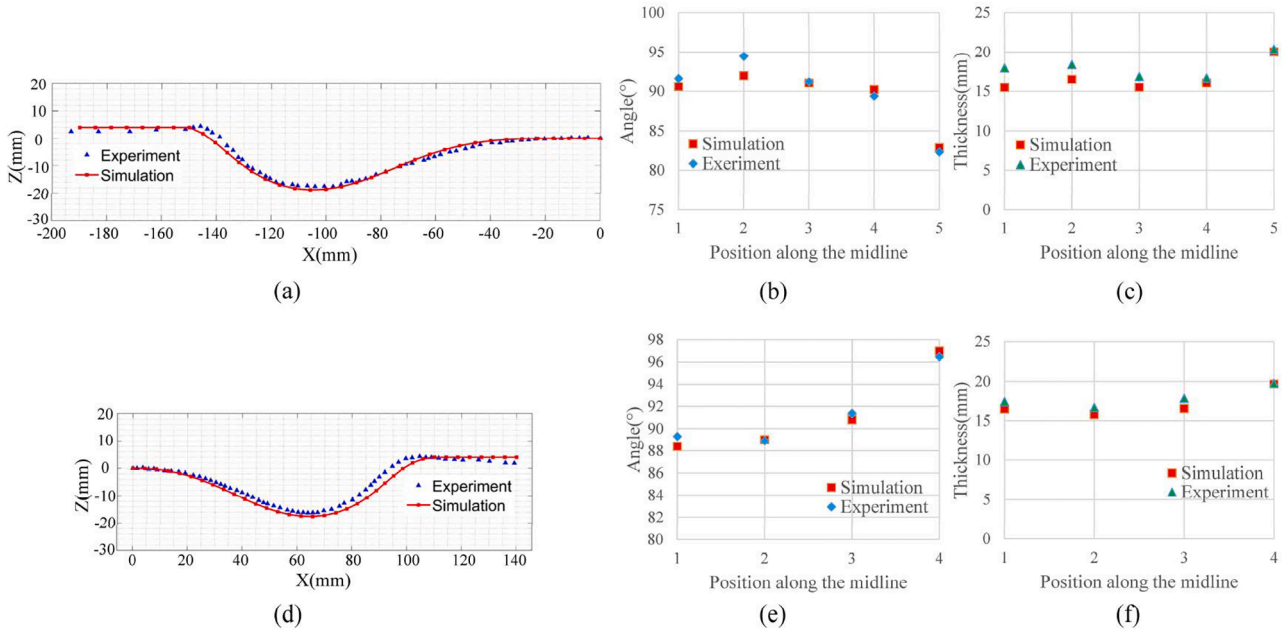

Fig. 16. Buckling bending test of a G1151 laminate. Deformed shape along side 1. (a) Experiment. (b) Simulation. Deformed shape along side 2. (c) Experiment. (d) Simulation. (For interpretation of the references to colour in this figure legend, the reader is referred to the web version of this article.)

corresponding simulation is presented (Fig. 15b and d). The deformed middle surface, the material director directions and thicknesses are shown in Fig. 16. The simulation shows a fairly good agreement with experiment.

6.3. Scope and limits of the approach

The proposed approach is developed for fibrous reinforcements with two directions of inextensible fibres in the plane of the reinforcement. This is an idealized situation. A real reinforcement, more or less deviates from this situation. Simulations based on this approach will be more relevant if one is close to this situation. Deformations of woven reinforcements and stacks of woven reinforcements are simulated in this paper with a correct agreement with the experiments (Figs. 6, 13, 15). The modelling can be satisfactorily extended to more complex reinforcements, e.g. thick interlocks [29]. However, the deformation of some 3D reinforcements containing tows in the thickness direction cannot be simulated with the proposed shell approach.

7. Conclusion

A shell approach specific to fibrous reinforcements is necessary because classical theories such as Kirchhoff and Mindlin are based on kinematic assumptions that are not verified for textile reinforcements. The deformation of these fibrous fabrics has two major features: the inextensibility of the fibres and the possible slippage between the fibres. A shell approach has been developed to take these specificities into account. An Ahmad shell finite element has been developed. This element has been validated on some 3D deformation tests where it has been shown that it allows determining the displacement, the strains at all points in the thickness and the rotation of the material normals in good coherence with the experiments. A simple approach was used to take into account friction between layers. The bending stiffness was measured on the overall reinforcement, and friction increases the bending stiffness, which is taken into account. Other ways can be considered to take friction into account, for example by adding a specific term in the virtual work. The proposed approach makes it possible to greatly reduce the cost of the calculations compared to an approach where each layer is described by a layer of shell finite elements in contact with its neighbours. Some aspects remain to be studied and modelled, in particular the case of the different orientations of the fibre plies in the textile reinforcement and the consideration of thickness variations during consolidation.

CRediT authorship contribution statement

Renzi Bai: Investigation, Methodology, Software, Validation, Visualization. **Julien Colmars:** Investigation, Methodology, Supervision. **Naim Naouar:** Supervision. **Philippe Boisse:** Conceptualization, Methodology, Supervision.

Declaration of Competing Interest

The authors declare that they have no known competing financial interests or personal relationships that could have appeared to influence the work reported in this paper.

Acknowledgements

This work was supported by the French Ministry of Higher Education and Research.

Appendix A

The lumped matrix for node k of the shell is given bellow, where k is the index number of node, ρ is the mass density of the element material, V is the volume of the element [50].

$$[M_k] = \begin{bmatrix} m_{kk} & 0 & 0 & 0 & 0 \\ 0 & m_{kk} & 0 & 0 & 0 \\ 0 & 0 & m_{kk} & 0 & 0 \\ 0 & 0 & 0 & I_{kk} & 0 \\ 0 & 0 & 0 & 0 & I_{kk} \end{bmatrix} \tag{38}$$

$$m_{ii} = \frac{\int_V \rho N_i(\xi,\eta)^T N_i(\xi,\eta) dV}{\sum_{k=1}^{3} \int_V \rho N_k(\xi,\eta)^T N_k(\xi,\eta) dV} \int_V \rho dV \text{ and } I_{ii} = \frac{m_{ii}}{4}(h_m^i)^2 \tag{39}$$

References

[1] Arbter R, Beraud JM, Binetruy C, Bizet L, Bréard J, Comas-Cardona S, et al. Experimental determination of the permeability of textiles: a benchmark exercise. Compos A Appl Sci Manuf 2011;42(9):1157–68.

[2] Sozer EM, Simacek P, Advani SG. Resin transfer molding (RTM) in polymer matrix composites. In: Manufacturing techniques for polymer matrix composites (PMCs). Woodhead Publishing; 2012. p. 245–309.

[3] Caglar B, Orgéas L, Du Roscoat SR, Sozer EM, Michaud V. Permeability of textile fabrics with spherical inclusions. Compos A Appl Sci Manuf 2017;99:1–14.

[4] Lukaszewicz DJ, Potter KD. The internal structure and conformation of prepreg with respect to reliable automated processing. Compos A Appl Sci Manuf 2011;42(3):283–92.

[5] Guzman-Maldonado E, Hamila N, Boisse P, Bikard J. Thermomechanical analysis, modelling and simulation of the forming of pre-impregnated thermoplastics composites. Compos A Appl Sci Manuf 2015;78:211–22.

[6] Lessard H, Lebrun G, Benkaddour A, Pham XT. Influence of process parameters on the thermostamping of a [0/90] 12 carbon/polyether ether ketone laminate. Compos A Appl Sci Manuf 2015;70:59–68.

[7] Levy A, Hubert P. Vacuum-bagged composite laminate forming processes: Predicting thickness deviation in complex shapes. Compos A Appl Sci Manuf 2019;126.

[8] Henning F, Kärger L, Dörr D, Schirmaier FJ, Seuffert J, Bernath A. Fast processing and continuous simulation of automotive structural composite components. Compos Sci Technol 2019;171:261–79.

[9] Van Der Weeën F. Algorithms for draping fabrics on doubly-curved surfaces. Int J Numerical Methods Eng 1991;31(7):1415–26.

[10] Long AC, Rudd CD. A simulation of reinforcement deformation during the production of preforms for liquid moulding processes. Proc Inst Mech Engineers, Part B: J Eng Manufacture 1994;208(4):269–78.

[11] Potluri P, Ciurezu DP, Ramgulam RB. Measurement of meso-scale shear deformations for modelling textile composites. Compos A Appl Sci Manuf 2006;37(2):303–14.

[12] Hancock SG, Potter KD. The use of kinematic drape modelling to inform the hand lay-up of complex composite components using woven reinforcements. Compos A Appl Sci Manuf 2006;37(3):413–22.

[13] Cherouat A, Billoët JL. Mechanical and numerical modelling of composite manufacturing processes deep-drawing and laying-up of thin pre-impregnated woven fabrics. J Mater Process Technol 2001;118(1–3):460–71.

[14] Ten Thije RHW, Akkerman R, Huétink J. Large deformation simulation of anisotropic material using an updated Lagrangian finite element method. Comput Methods Appl Mech Eng 2007;196(33–34):3141–50.

[15] Lin H, Wang J, Long AC, Clifford MJ, Harrison P. Predictive modelling for optimization of textile composite forming. Compos Sci Technol 2007;67(15–16):3242–52.

[16] Chen S, Harper LT, Endruweit A, Warrior NA. Formability optimisation of fabric preforms by controlling material draw-in through in-plane constraints. Compos A Appl Sci Manuf 2015;76:10–9.

[17] Chen S, McGregor OPL, Harper LT, Endruweit A, Warrior NA. Defect formation during preforming of a bi-axial non-crimp fabric with a pillar stitch pattern. Compos A Appl Sci Manuf 2016;91:156–67.

[18] Boisse P, Hamila N, Vidal-Sallé E, Dumont F. Simulation of wrinkling during textile composite reinforcement forming. Influence of tensile, in-plane shear and bending stiffnesses. Compos Sci Technol 2011;71(5):683–92.

[19] Dangora LM, Mitchell CJ, Sherwood JA. Predictive model for the detection of out-of-plane defects formed during textile-composite manufacture. Compos A Appl Sci Manuf 2015;78:102–12.

[20] Lomov SV, Truevtzev AV, Cassidy C. A predictive model for the fabric-to-yarn bending stiffness ratio of a plain-woven set fabric. Text Res J 2000;70(12):1088–96.

[21] Yu WR, Zampaloni M, Pourboghrat F, Chung K, Kang TJ. Analysis of flexible bending behavior of woven preform using non-orthogonal constitutive equation. Compos A Appl Sci Manuf 2005;36(6):839–50.

[22] Döbrich O, Gereke T, Diestel O, Krzywinski S, Cherif C. Decoupling the bending behavior and the membrane properties of finite shell elements for a correct description of the mechanical behavior of textiles with a laminate formulation. J Ind Text 2014;44(1):70–84.

[23] Nishi M, Hirashima T, Kurashiki T. Dry fabric forming analysis considering the influence of tensions on in-plane shear behavior. J Soc Mater Sci, Japan 2014;63(5):380–5.

[24] Yu F, Chen S, Viisainen JV, Sutcliffe MPF, Harper LT, Warrior NA. A macroscale finite element approach for simulating the bending behaviour of biaxial fabrics. Compos Sci Technol 2020;191.

[25] Hamila N, Boisse P, Sabourin F, Brunet M. A semi-discrete shell finite element for textile composite reinforcement forming simulation. Int J Numer Meth Eng 2009;79(12):1443–66.

[26] Schirmaier FJ, Dörr D, Henning F, Kärger L. A macroscopic approach to simulate the forming behaviour of stitched unidirectional non-crimp fabrics (UD-NCF). Compos A Appl Sci Manuf 2017;102:322–35.

[27] Haanappel SP, Ten Thije RHW, Sachs U, Rietman B, Akkerman R. Formability analyses of uni-directional and textile reinforced thermoplastics. Compos A Appl Sci Manuf 2014;56:80–92.

[28] Dörr D, Henning F, Kärger L. Nonlinear hyperviscoelastic modelling of intra-ply deformation behaviour in finite element forming simulation of continuously fibre-reinforced thermoplastics. Compos A Appl Sci Manuf 2018;109:585–96.

[29] Liang B, Colmars J, Boisse P. A shell formulation for fibrous reinforcement forming simulations. Compos A Appl Sci Manuf 2017;100:81–96.

[30] Ahmad S, Irons BM, Zienkiewicz OC. Analysis of thick and thin shell structures by curved finite elements. Int J Numer Meth Eng 1970;2(3):419–51.

[31] Dvorkin EN, Bathe KJ. A continuum mechanics based four-node shell element for general non-linear analysis. Eng Computations 1984;1:77–88.

[32] Parisch H. A continuum-based shell theory for non-linear applications. Int J Numerical Methods Eng 1995;38(11):1855–83.

[33] Auricchio F, Taylor RL. A triangular thick plate finite element with an exact thin limit. Finite Elem Anal Des 1995;19(1–2):57–68.

[34] O.C. Zienkiewicz, R.L. Taylor, The finite element method for solid and structural mechanics, Elsevier, 2005.

[35] J.L. Batoz, G. Dhatt, Modélisation des structures par éléments finis: Volume 2 : Poutres et plaques, Presses Université Laval, 1990.

[36] Creech G, Pickett AK. Meso-modelling of non-crimp fabric composites for coupled drape and failure analysis. J Mater Sci 2006;41(20):6725–36.

[37] Pazmino J, Mathieu S, Carvelli V, Boisse P, Lomov SV. Numerical modelling of forming of a non-crimp 3D orthogonal weave E-glass composite reinforcement. Compos A Appl Sci Manuf 2015;72:207–18.

[38] Mathieu S, Hamila N, Bouillon F, Boisse P. Enhanced modeling of 3D composite preform deformations taking into account local fiber bending stiffness. Compos Sci Technol 2015;117:322–33.

[39] El Said B, Daghia F, Ivanov D, Hallett SR. An iterative multiscale modelling approach for nonlinear analysis of 3D composites. Int J Solids Struct 2018;132:42–58.

[40] Ten Thije RHW, Akkerman R. Solutions to intra-ply shear locking in finite element analyses of fibre reinforced materials. Compos A Appl Sci Manuf 2008;39(7):1167–76.

[41] Hamila N, Boisse P. Locking in simulation of composite reinforcement deformations. Analysis and treatment. Compos A Appl Sci Manuf 2013;53:109–17.

[42] Harrison P, Clifford MJ, Long AC. Shear characterisation of viscous woven textile composites: a comparison between picture frame and bias extension experiments. Compos Sci Technol 2004;64(10–11):1453–65.

[43] Boisse P, Zouari B, Daniel JL. Importance of in-plane shear rigidity in finite element analyses of woven fabric composite preforming. Compos A Appl Sci Manuf 2006;37(12):2201–12.

[44] Cao J, Akkerman R, Boisse P, Chen J, Cheng HS, De Graaf EF, Lee W. Characterization of mechanical behavior of woven fabrics: experimental methods and benchmark results. Compos A Appl Sci Manuf 2008;39(6):1037–53.

[45] Na W, Ahn H, Han S, Harrison P, Park JK, Jeong E, Yu WR. Shear behavior of a shear thickening fluid-impregnated aramid fabrics at high shear rate. Compos B Eng 2016;97:162–75.

[46] Hamila N, Boisse P. A meso–macro three node finite element for draping of textile composite preforms. Appl Compos Mater 2007;14(4):235–50.

[47] T. Belytschko, An overview of semidiscretization and time integration procedures, Computational methods for transient analysis(A 84-29160 12-64), Amsterdam, North-Holland, 1983, pp. 1-65.

[48] Hughes TJR, Belytschko T. A precis of developments in computational methods for transient analysis. ATJAM 1983;50:1033–41.

[49] M.A. Crisfield, Non-linear Finite Element Analysis of Solids and Structures: Advanced Topics. Bol. 2, John Wiley & Sons, 1997.

[50] Surana KS. Lumped mass matrices with non− zero inertia for general shell and axisymmetric shell elements. Int J Numer Meth Eng 1978;12(11):1635–50.

[51] Onate E, Zárate F. Rotation-free triangular plate and shell elements. Int J Numerical Methods Eng 2000;47(1–3):557–603.

[52] Sabourin F, Brunet M. Detailed formulation of the rotation-free triangular element "S3" for general purpose shell analysis. Eng Computations 2006.
[53] Brunet M, Sabourin F. Analysis of a rotation-free 4-node shell element. Int J Numerical Methods Eng 2006;66(9):1483–510.
[54] Boisse P, Colmars J, Hamila N, Naouar N, Steer Q. Bending and wrinkling of composite fiber preforms and prepregs. A review and new developments in the draping simulations. Compos B Eng 2018;141:234–49.
[55] Naouar N, Vidal-Sallé E, Schneider J, Maire E, Boisse P. Meso-scale FE analyses of textile composite reinforcement deformation based on X-ray computed tomography. Compos Struct 2014;116:165–76.
[56] Vanclooster K, Lomov SV, Verpoest I. Simulation of multi-layered composites forming. Int J Mater Form 2010;3(1):695–8.
[57] Fetfatsidis KA, Jauffrès D, Sherwood JA, Chen J. Characterization of the tool/fabric and fabric/fabric friction for woven-fabric composites during the thermostamping process. Int J Mater Form 2013;6(2):209–21.
[58] Guzman-Maldonado E, Wang P, Hamila N, Boisse P. Experimental and numerical analysis of wrinkling during forming of multi-layered textile composites. Compos Struct 2019;208:213–23.
[59] Chakladar ND, Mandal P, Potluri P. Effects of inter-tow angle and tow size on carbon fibre friction. Compos A Appl Sci Manuf 2014;65:115–24.
[60] De Bilbao E, Soulat D, Hivet G, Gasser A. Experimental study of bending behaviour of reinforcements. Exp Mech 2010;50(3):333–51.
[61] Allaoui S, Boisse P, Chatel S, Hamila N, Hivet G, Soulat D, Vidal-Salle E. Experimental and numerical analyses of textile reinforcement forming of a tetrahedral shape. Compos A Appl Sci Manuf 2011;42(6):612–22.
[62] Gherissi A, Abbassi F, Ammar A, Zghal A. Numerical and experimental investigations on deep drawing of G1151 carbon fiber woven composites. Appl Compos Mater 2016;23(3):461–76.